ELSEVIER

International Journal of Pharmaceutics 142 (1996) 33–51

international journal of pharmaceutics

Numerical analysis of motion and deposition of particles in cascade impactors

P.D. Swanson[a], F.J. Muzzio[a,*], A. Annapragada[b], A. Adjei[b]

[a]*Department of Chemical and Biochemical Engineering, Rutgers University, Piscataway, NJ 08855, USA*
[b]*Abbott Laboratories, North Chicago, IL 60064, USA*

Received 17 July 1995; revised 3 June 1996; accepted 18 June 1996

Abstract

The motion and deposition of small solid particles (1–10μm) in an idealized six-stage cascade impactor is investigated numerically. The flow of air is simulated using commercial software, and the trajectories of solid particles are predicted by integrating equations of motion that include gravitational forces, inertia and viscous friction. Particle–wall interactions are modeled in terms of a sticking probability and a restitution coefficient. The model correctly predicts the typical S-shaped trapping efficiency curves. As expected, the sticking probability has the greatest impact on trapping profiles. The restitution coefficient has only a very small effect, which becomes negligible for large sticking probability. However, a large unanticipated effect is uncovered by the model. The flow inside the impactor displays large recirculation regions that act as efficient traps of particles of specific sizes. Particles trapped in these regions do not deposit on collection plates, possibly biasing analysis results. This effect, which is magnified at low sticking probabilities, provides an alternative explanation for the 'wall losses' reported in several experimental studies that have examined impactors similar to the one studied here.

Keywords: Particle size measurement; Cascade impactors; Aerosolized medications

1. Introduction and literature review

Since their introduction by May (1945), cascade impactors have gained acceptance as a convenient means to characterize the size distribution of aerosol particles. Marple (1970) laid the computational foundation for the systematic study and design of these devices. In a cascade impactor, a gaseous sample containing the particles of interest is drawn through a sampling port into a series of chambers connected by successively smaller orifices. As the aerosol particles flow through the orifices ('stages') of the device, they are propelled toward collection plates with increasingly larger inertia. If a particle has sufficient inertia, it col-

* Corresponding author.

PII S0378-5173(96)04643-1

lides with the collection plate; if not, it is swept aside by the air flow. Once the sampling is complete, the amount of material deposited on each plate is determined. The measurement results in a characterization of the size distribution of the particles in the gaseous stream, although the size range of particles deposited on each plate usually requires experimental calibration or reliance on information provided by the device's manufacturer.

Applications of this technique are found in a wide range of fields, including measurements on adventitious airborne particles and pollutants (Marple et al., 1991; Hecht and Cibulsky, 1992), coal dusts (Ondov et al., 1975), airborne allergens (Luczynska et al., 1990) and automotive exhaust particles (Goto et al., 1987). In the recent past, with the development of aerosolized medications, impactors have become a popular method of characterizing the size distributions of aerosolized drug particles (Fults et al., 1991). These studies have been motivated by the widely held belief that the size of a particle is the primary determinant of its fate when introduced into the respiratory tract (Holzner and Muller, 1995). It is believed that particles larger than a given size will be deposited in the upper portions of the tract, while particles below this size will succeed in penetrating the deep lung and deposit in the alveoli. Since impactor methods are all based on the entrainment of particles in an air stream, it is natural to suggest that the behavior of particles in an impaction device can be correlated to their behavior in the respiratory tract.

Cascade impactors are increasingly gaining acceptance by regulatory agencies. A variety of devices are currently available from several manufacturers. Each of these instruments has different physical dimensions, and each one provides a different size distribution characterization. An important but seldom studied factor affecting the performance of impactors is the global flow pattern inside them. Depending on the global flow characteristics of a given device, particles can fail to impact the collection surfaces. This phenomenon is commonly referred to as 'wall losses' and was already recognized as a source of error in the earliest studies on cascade impactors (May, 1945). Several studies have shown that such losses can be very substantial for particles in the 1–10-μm size range (Fairchild and Wheat, 1984; Horton et al., 1992). However, there has been little fundamental study on how global flow through an impactor and particle–wall interactions result in these losses, and how those losses become compounded by combination of effects through several stages.

Numerical simulations are used here to address such issues. Previous numerical analysis of flow in cascade impactors has been limited to either the behavior of a single jet impinging on a surface (Marple and Liu, 1974; Rader and Marple, 1985; Jurcik et al., 1989; Her and Kim, 1991) or the convolution of empirically determined single-stage data into the behavior of a multi-stage device (Natusch and Wallace, 1976; Vaughan, 1989). This paper presents a detailed numerical analysis of the flow in an entire impactor that is similar to a popular, commercially available device (California Measurements PC-2) (Fairchild and Wheat, 1984; Horton et al., 1992; Hering, 1987). The geometry of the simulated system (Fig. 1) is described in Section 2. The velocity field of the fluid phase is examined in Section 3. The numerical algorithm used to simulate the trajectories of solid particles is presented in Section 4. A detailed analysis of the fluid and particle dynamics is presented in these sections. Interactions between particles and solid surfaces are represented by two parameters: a sticking probability and a restitution coefficient. Computations of this nature allow us to calculate a priori the cutoff diameters for each stage. Such information is also presented in Section 5. In Section 6, results obtained from simulations considering a large number particles with a realistic distribution of sizes are presented. Conclusions and future work are discussed in Section 7.

2. System

The cascade impactor considered in this paper is illustrated in Fig. 1. The system is an idealized version of the first six stages of the California Instruments PC-2 impactor (California Measure-

ments, Sierra Madre, CA). This system is regarded as a good case study for the numerical analysis of global flow in an entire cascade impactor. Its axisymmetric geometric greatly simplifies numerical simulation of the flow. The instrument is basically a cylindrical pipe with cross-sectional collection stages. A collection stage has two components: (i) a large plate spanning the entire cross-section of the pipe, transversed by a single central hole parallel to the pipe's axis and (ii) a small collection plate placed downstream from the hole, orthogonal to the pipe's axis. Small internal features such as microbalances and wires are neglected in the analysis. The physical dimensions of the system are defined in Fig. 1.

An aerosol enters the system from the top. As the aerosol flows through the hole, jets impinge on the collection plates. Depending on their inertia, particles will either collide with the collection plate or be swept aside by the air flow. The diameter of the holes decreases in the downstream direction (Fig. 1), increasing the intensity of each subsequent jet. This increases the inertia of particles (and hence their momentum), increasing the probability that they will collide with the collection plate.

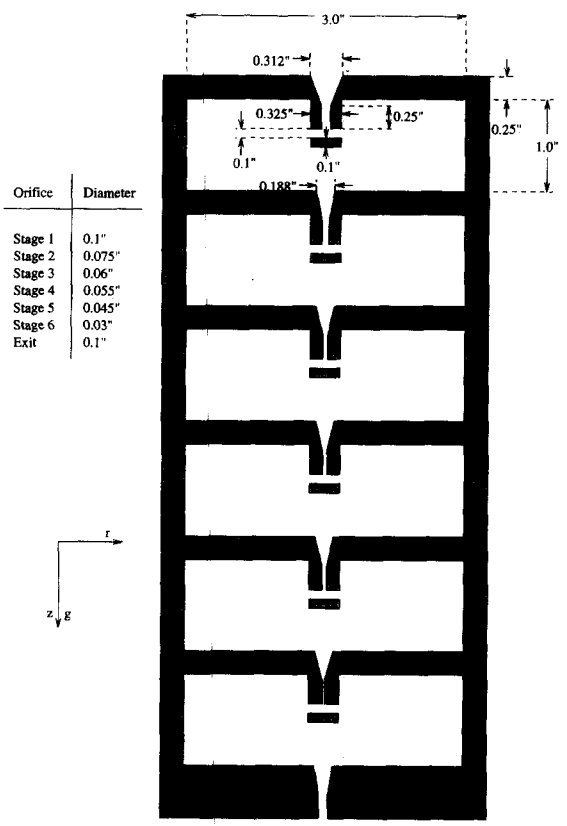

Fig. 1. Geometry of the idealized six-stage cascade impactor considered in this paper.

3. Velocity field

The velocity field of the air–solid suspension is determined using a commercial software package (FLUENT UNS 1.0, Fluent, Lebanon, NH). This commercial package, used in combination with a mesh generator, provides an efficient approach for computation of the velocity field in systems with a moderate level of geometric complexity. Such commercial software packages have recently become a popular tool due to their simplicity and effectiveness (Yang et al., 1993; Dupont et al., 1993; Sazhin et al., 1993). Simulations are restricted to conditions where the solid particles are a small fraction of the total mass of the suspension (less than 1%). Under such conditions, it can be assumed that the velocity of air is not affected significantly by the presence of solid particles. The independent variables in the simulation are the pressure and temperature conditions for the air entering the device (standard conditions are assumed throughout this paper), the flow rate of air entering the device (computed as the integral of the velocity across the entrance) and the geometry of the system (Fig. 1). Once these parameters are specified, the system has no degrees of freedom, and all other quantities (density, air velocity, discharge pressure, particle trajectories) are regarded as dependent variables and are determined from the simulation (details are provided below). Choosing the flow rate as an independent variable reflects the usual practice in the operation of these devices; typically, the flow is driven by a vacuum pump placed at the discharge of the system, and the flow rate is adjusted to a desired value by opening or closing a valve located between the impactor and the pump.

A detailed description of the fluid and particle dynamics, including the assumptions that are re-

quired to obtain a numerical solution of the flow in the device, is presented next. The system is described using a cylindrical coordinate system (r, z, θ) to take full advantage of symmetries in the flow geometry. In principle, one needs to solve the three-dimensional non-linearly coupled partial differential mass and momentum balances (Bird et al., 1960):

$$\partial\rho/\partial t = -(1/r)\,\partial(\rho r u_r)/\partial r - \partial(\rho u_z)/\partial z - (1/r)\,\partial(\rho u_\theta)/\partial\theta, \tag{1a}$$

$$\rho[\partial u_r/\partial t + u_r\,\partial u_r/\partial r + u_z\,\partial u_r/\partial z + (u_\theta/r)\,\partial u_r/\partial\theta - u_\theta^2/r] = -\partial P/\partial r - (1/r)\,\partial(r\tau_{rr})/\partial r - \partial\tau_{rz}/\partial z - (1/r)\,\partial\tau_{r\theta}/\partial\theta + \tau_{\theta\theta}/r + \rho g_r, \tag{1b}$$

$$\rho[\partial u_z/\partial t + u_r\,\partial u_z/\partial r + u_z\,\partial u_z/\partial z + (u_\theta/r)\,\partial u_z/\partial\theta] = -\partial P/\partial z - (1/r)\,\partial(r\tau_{rz})/\partial r - \partial\tau_{zz}/\partial z - (1/r)\,\partial\tau_{z\theta}/\partial\theta + \rho g_z, \tag{1c}$$

$$\rho[\partial u_\theta/\partial t + u_r\,\partial u_\theta/\partial r + u_z\,\partial u_\theta/\partial z + (u_\theta/r)\,\partial u_\theta/\partial\theta + (u_\theta/u_r)/r] = -(1/r)\,\partial P/\partial\theta - (1/r^2)\,\partial(r^2\tau_{r\theta})/\partial r - \partial\tau_{z\theta}/\partial z - (1/r)\,\partial\tau_{\theta\theta}/\partial\theta + \rho g_\theta, \tag{1d}$$

where Eq. (1a) is the mass balance; Eqs. (1b–d) are the r, z, and θ components of the momentum balance; u_r, u_z, and u_θ are the components of the velocity in the r, z, and θ directions; P is pressure; g_r, g_z, and g_θ are the components of the gravity vector; and the terms τ_{ij} are the components of the stress tensor. However, since the flow geometry and boundary conditions are axisymmetric and the Reynolds number is moderate[1], the angular coordinate θ can be neglected, i.e. the velocity component u_θ, all derivatives with respect to θ, and all components $\tau_{i\theta}$ can be neglected. Since the axis of impactor is considered to be parallel to the vertical direction, $g_r = g_\theta = 0$. With these assumptions, the problem is reduced to solving the steady two-dimensional compressible flow in r and z given by

$$0 = -(1/r)\,\partial(r\rho u_r)/\partial r - \partial(\rho u_z)/\partial z, \tag{2a}$$

$$\rho[u_r\,\partial u_r/\partial r + u_z\,\partial u_r/\partial z] = -\partial P/\partial r - (1/r)\,\partial(r\tau_{rr})/\partial r - \partial\tau_{rz}/\partial z, \tag{2b}$$

$$\rho[u_r\,\partial u_z/\partial r + u_z\,\partial u_z/\partial z] = -\partial P/\partial z - (1/r)\,\partial(r\tau_{zr})/\partial r - \partial\tau_{zz}/\partial z + \rho g_z, \tag{2c}$$

Non-slip boundary conditions,

$$u_r = 0, \qquad u_z = 0, \tag{3a}$$

are used for all solid surfaces, and a symmetry boundary condition,

$$u_r = 0, \qquad \partial u_z/\partial z = 0, \tag{3b}$$

is used for the axis of the flow region ($r = 0$).

These equations were solved using the above-mentioned software package, which employs a modern finite-element/finite-volume algorithm to ensure accurate solution of Eqs. (2a–c). Convergence of the solution was achieved by using the usual approach of increasing the number of nodes until the solution became independent of the number of nodes. In the final solution thus obtained, the axial (r, z) half plane of the flow domain is discretized using an array of 25 384 nodal points arranged in an unstructured grid of 11 747 triangular elements generated using a commercial grid generator (PREBFC 4.3.1, Fluent Lebanon, NH). Such unstructured grids yield results that are considerably more accurate than those generated by the structured grids used in early studies (Marple, 1970; Marple and Liu, 1974; Rader and Marple, 1985). The density of nodes is non-uniform; nodes are placed more densely in the holes and close to the solid walls to resolve accurately the larger velocity gradients that occur at such locations. The entire mesh is displayed in Fig. 2(a) and a detail of the grid in the hole-and-plate region of the first section is shown in Fig. 2(b).

In the remainder of this section, we describe results obtained for a total air flow rate of 240 standard cc/min, which is the manufacturer's recommended flow rate for a California Instruments

[1] The Reynolds number based on the flow through each hole is $\mathrm{Re} = \rho V d/\mu$, where ρ is the air density, μ is the air viscosity, V is the average velocity through the hole, and d is the hole diameter. Re is largest for the last hole, and for the flow considered here is always less than 500.

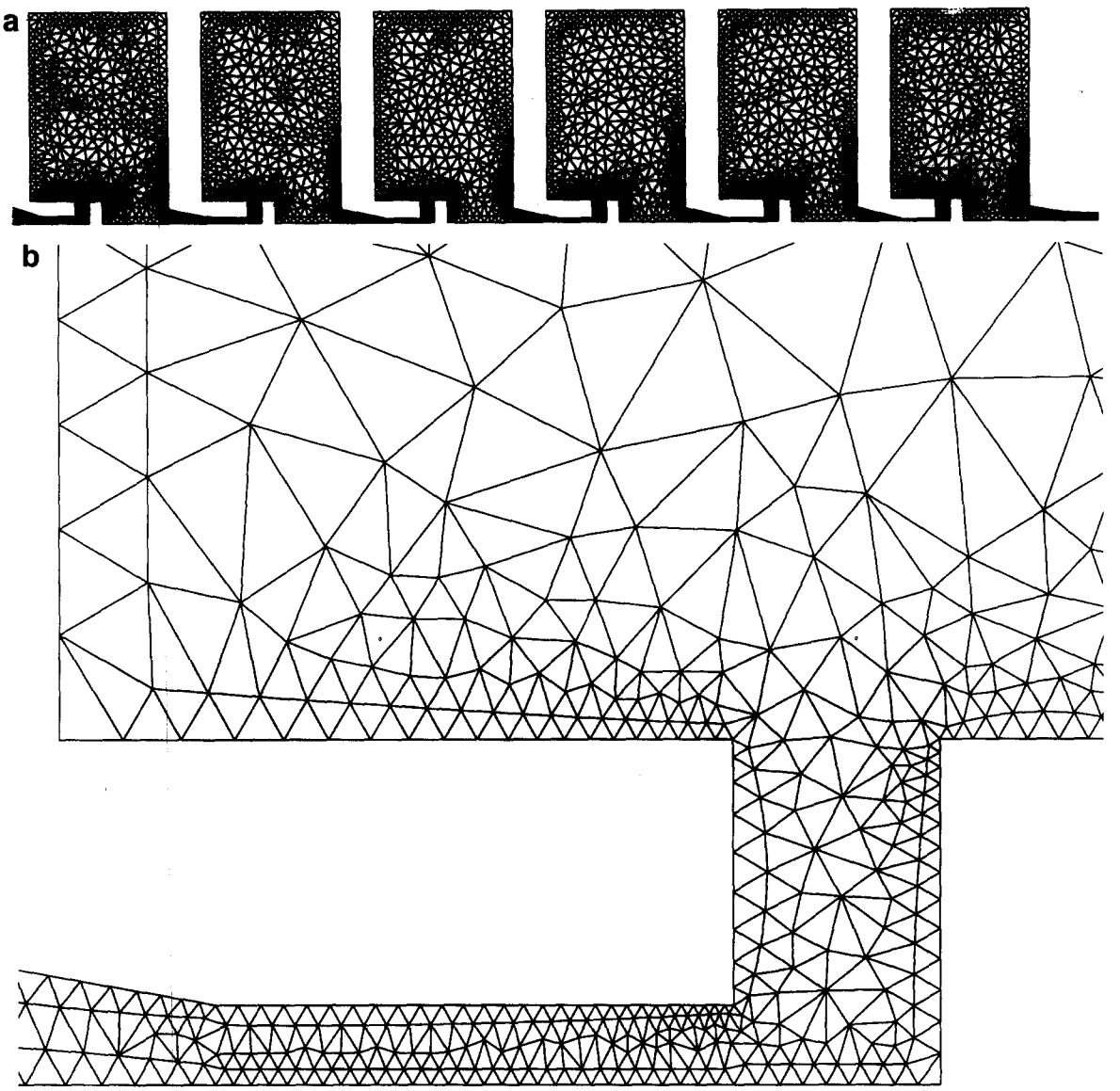

Fig. 2. (a) Unstructured mesh of nodal points used for the finite-element determination of the velocity field inside the impactor. (b) Detail of the mesh in the hole-and-plate region.

impactor of dimensions similar to those of the device examined in our simulations. This flow rate was specified by adjusting the velocity at the entrance of the device until a surface integral of the velocity generated the desired flow rate. Fig. 3(a) shows the velocity field predicted by FLUENT for the entire device. The points are color coded in the following sequence according to the magnitude of the velocity (from high to low): red, yellow, light blue and dark blue. Colors are assigned ad-hoc to enhance visual display of the results. Regions of fast flow (such as the holes) correspond to red and yellow regions. As air flows through the convergent section of the hole, an axial jet of nearly uniform intensity develops. The jet impinges onto the plate nearly vertically, where it is deflected into the chamber.

The flow in the rest of the system is much weaker, and has a complex structure, also revealed in the streamline portrait of the entire device (Fig. 3(b)). Flow through the chamber of each stage is highly stratified and is hindered by the presence of two coherent recirculation vortices. The structure of these vortices is sketched in Fig. 3(c). A relatively small vortex dominates the flow region immediately above each collection plate. This flow region is bounded by a streamline that separates at corner A and reattaches at point B. Another, very large vortex, is bounded by a streamline that separates at corner C, goes around most of chamber, and reattaches itself to corner D. Since fluid cannot cross streamlines (solid particles can, however, and do), all of the air flows through the region outside the vortices in Fig. 3(c).

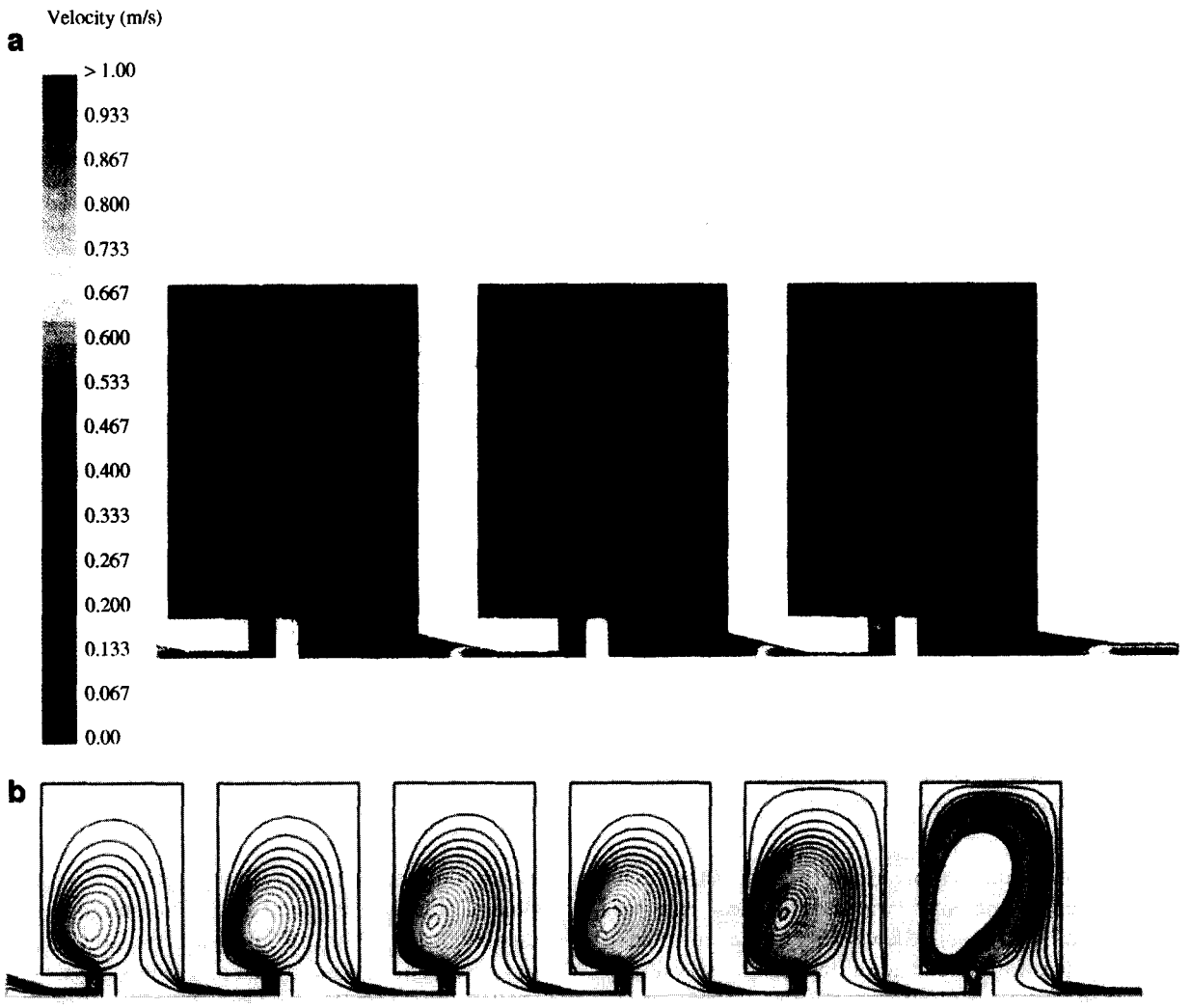

Fig. 3. (a) The colors represent the intensity of the velocity field, in decreasing order of red, yellow, light blue and dark blue. (b) Stream function contours indicating the trajectories of fluid particles. (c) Sketch of the flow structure, indicating the topology of recirculating flow regions bounded by closed streamlines.

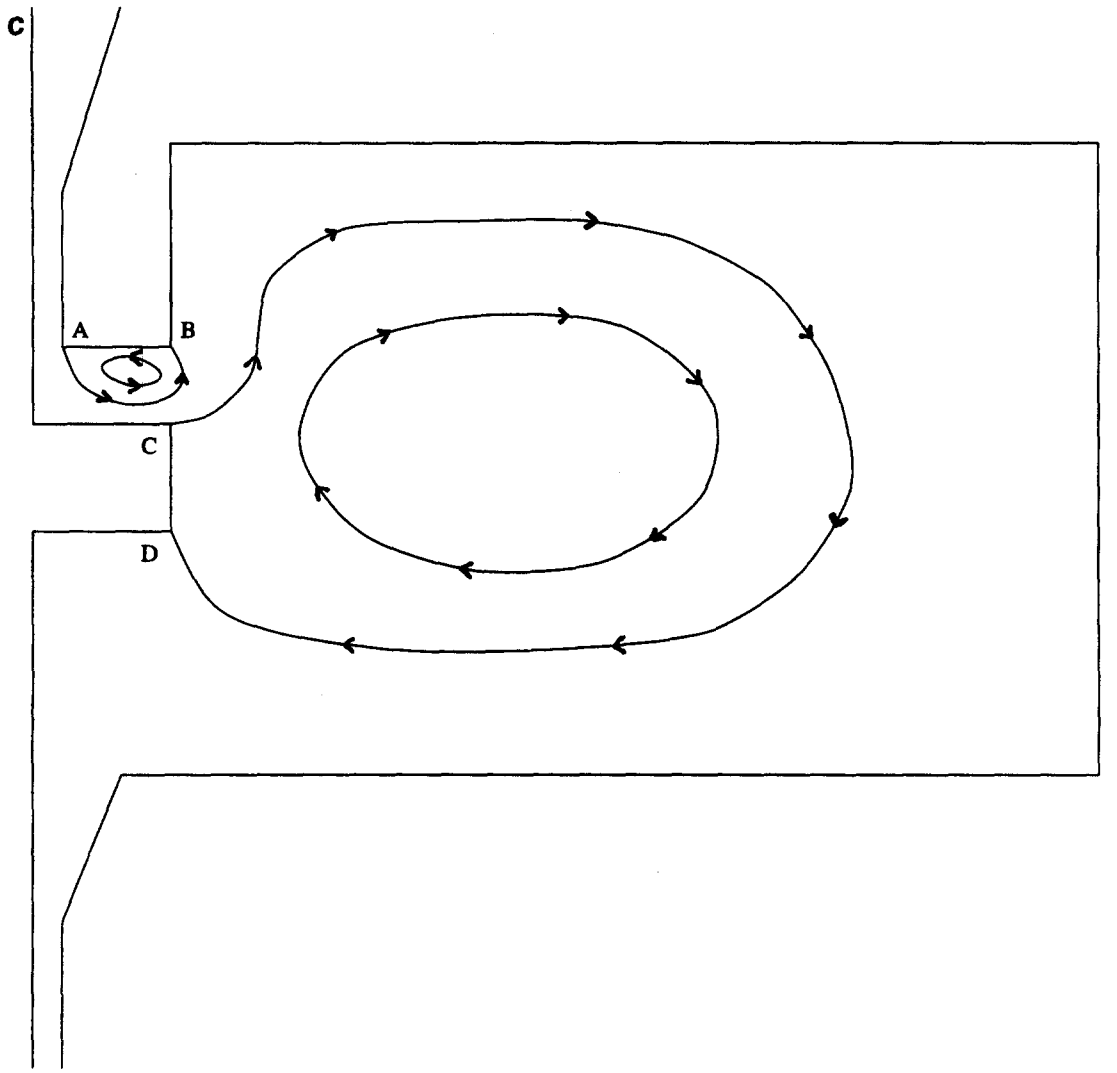

Fig. 3(c).

4. Motion of solid particles in the impactor

The motion of solid particles suspended in a fluid has been investigated in many previous studies (Liu and Peskin, 1993; Druzhinin et al., 1993; Sommerer and Ott, 1993; Tio et al., 1993; Wang et al., 1992; Yu et al., 1991). It is generally recognized that the forces acting on discrete solid particles are different, and more complex, than those acting on the fluid. In principle, the equation of motion for particles should account for the effects of buoyancy, inertia and drag forces (Liu and Peskin, 1993; Maxey and Riley, 1983). These forces appear as velocity-dependent dissipative terms in the equation of motion (Maxey and Riley, 1983):

$$m_p\, d\boldsymbol{v}/dt = (m_p - m_F)\boldsymbol{g} + m_F\, D\boldsymbol{u}/Dt - 6\pi a^2\mu \int [\pi\nu(t-t')]^{-1/2}(d\boldsymbol{X}/dt)\, dt' - (1/2)m_F\, d[\boldsymbol{v} - \boldsymbol{u} - (1/10)a^2\nabla^2\boldsymbol{u}]/dt - 6\pi a\mu\boldsymbol{X}, \quad (4)$$

where $\mathbf{X} = \mathbf{v} - \mathbf{u} - (1/6)a^2\nabla^2\mathbf{u}$.

In Eq. (4), **u** is the fluid velocity, **v** is the particle velocity, a is the particle diameter, μ is the dynamic viscosity, and ν $(=\rho/\mu)$ is the kinematic viscosity; m_p and m_F respectively correspond to the weight of the particle and that of the fluid displaced by the particle. The five terms on the right hand side of the equation correspond, respectively, to buoyancy forces, pressure forces, flow history effects, added mass effect, and Stokes drag forces. This approach neglects discrete effects such as particle–particle interactions and particle Brownian motion. Particle–particle collisions can be safely neglected for the case considered in this paper due to laminar flow and the low volume fraction (less than 0.001%) of the solid phase. Brownian motion, on the other hand, could actually be important for small enough particles, and will be considered in future publications.

Eq. (4) can be significantly simplified for the impactor problem. Since **u** is known from the numerical solution of the flow, the relative magnitude of each term can be evaluated. Straightforward analysis shows that only inertia, buoyancy and drag forces need to be considered. All terms containing a^2 are negligible for small particles such as those considered here. Since, for an aerosol, the particle density is about 10^3 times larger than the fluid density, all terms containing m_F can also be neglected in Eq. (4). After applying these simplifications, one obtains

$$m_p \, d\mathbf{v}/dt = m_p \mathbf{g} - 6\pi a\mu[\mathbf{v} - \mathbf{u}], \tag{5}$$

which can be expressed in terms of non-dimensional time $(t' = tU/L)$ and velocities $(\mathbf{u}' = \mathbf{u}/U, \mathbf{v}' = \mathbf{v}/U)$ to give

$$d\mathbf{v}'/dt' = (1/\mathrm{Fr}) - (1/\mathrm{St})[\mathbf{v}' - \mathbf{u}'], \tag{6}$$

where Fr, the Froude number, represents the characteristic ratio of inertial forces to gravitational forces and is given by $\mathrm{Fr} = U^2/Lg$. St, the Stokes number, gives the ratio of inertial forces to viscous forces and is given by $\mathrm{St} = m_p U/(6\pi a\mu L)$; L is the characteristic length of the flow (in this case chosen arbitrarily to be equal to the diameter of the first hole), and U is the characteristic flow velocity (in this case chosen arbitrarily to be equal to the average velocity though the first hole). For the cases considered here, $\mathrm{Fr} \approx 25$ and $\mathrm{St} \approx 0.1$–0.001, suggesting that viscous transport of momentum from the fluid to the particles is the main force dominating particle trajectories. Note that this results in particle equations of motion equivalent to those used previously (Marple and Liu, 1974; Rader and Marple, 1985) but with the addition of gravity which could be important in the relatively slow-flowing inter-stage chambers.

Eq. (6) indicates that particle trajectories depend on three forces: gravity, particle inertia and friction with the fluid. Even under such simplified conditions, particles subjected to these forces can exhibit behaviors that are very different from those of infinitesimal, non-buoyant fluid particles. Accurate representation of the motion of the particles requires knowing both **u** and **v** at all times. The fluid velocity **u** is known at nodal points from the computation described in the previous section. As the particles travel through the region confined by a given set of nodal points, **u** is determined as a second-order interpolation of the values of **u** at the nodes. Particles are assumed to begin with zero velocity at the entrance of the first hole. Since particles of the sizes considered here have small values of St, they quickly adapt to the surrounding fluid, and the initial velocity is 'forgotten' long before the particles exit the first hole. Subsequently, **v** is determined by integrating Eq. (5) using a variable-time-step semi-implicit fourth-order Runge-Kutta algorithm (Stoer and Bulirsch, 1980). Particle trajectories are then predicted integrating **v** with respect to time, i.e. radial and axial position are determined as a function of time by using the same algorithm to integrate

$$dr/dt = v_r \qquad dz/dt = v_z, \tag{7}$$

The algorithm uses very small time steps in regions near walls in order to optimize the accuracy of the calculated trajectories near impaction plates. Trajectories and deposition patterns predicted by these algorithms are discussed in the remainder of this paper.

5. Effects of particle size and particle–wall interactions

Particle–wall interactions are the remaining major building block in the simulation. To have a complete algorithm, we need to describe not only the flow and the motion of particles but also the outcome of particle–wall collisions. Accurate description of such interactions is a complex problem that is an active area of research (Hinds et al., 1985; Xu et al., 1993; John, 1995; Dahneke, 1995; Dunn et al., 1995; Tsai and Cheng, 1995). In this paper, to maximize the number of particles that can be considered in the simulations, a particle is assumed to be affected by surfaces only when it touches them. Long-range interactions, such as electrostatic forces, are not considered. Particle–wall interactions are modeled in terms of two parameters: the sticking probability p_S, and the restitution coefficient R, which are considered as independent variables in the simulations and are independent of particle size. The sticking probability p_S is defined as an instantaneous trapping efficiency between 0 and 1. As particles exit a hole, some of them have sufficient inertia to collide with the collection plate. When such a collision occurs, a random number uniformly distributed between 0 and 1 is computed using a standard random number generator. If the number is smaller than p_S, the collision is deemed 'effective' and the particle sticks to the plate. As a result, the number of particles that stick to a plate after a collision is, in average, proportional to p_S. The same procedure is used to decide whether particles stick to other surfaces on the impactor. Ineffective collisions are modeled as partially elastic collisions. If a particle does not stick to the wall, it bounces back from the wall with a velocity normal to the plate that is equal in magnitude to the impinging normal velocity multiplied by the restitution coefficient (i.e. R is defined as the ratio of the velocity normal to the plate after the collision and before the collision); the velocity component tangential to the plate is assumed to remain unaffected by the collision. In general, a particle collides only once with a given collection plate; very few particles collide multiple times with the same plate. For simplicity, only the first collision between a given particle and a given collection plate is considered as potentially effective. The first collision occurs immediately after particles leave the hole, and particles hit the plate with a significant amount of momentum. In subsequent collisions (if any), particles are pulled slowly towards the plate by gravity, and collide with the plate with only a small amount of momentum. All such collisions are deemed ineffective and are ignored in the simulation.

The analysis of the effects of impactor geometry and particle–wall interactions on particle deposition begins with the computation of stage trapping curves. This computation attempts to recreate the standard tests reported in the literature (and also by manufacturers) to calibrate the cut-off sizes corresponding to each stage. Briefly, 1000 particles of a single diameter are uniformly distributed across the entrance to a stage. The particles then follow trajectories predicted by Eq. (7). Since the corresponding experiment is typically conducted using sticky (oil-coated) collection plates, in the simulation it is assumed that $p_S = 1.0$, i.e. every particle that touches the plate is assumed to stick to it. The number of particles that stick to the stage is recorded. The procedure is repeated 20 times using sets of 1000 particles with diameters 0.5, 1, 1.5, ..., 10 μm, generating a curve of trapping efficiency versus particle diameter. The trapping efficiency is defined as the fraction of particles of a given size trapped in the plate. To avoid interactions between stages, this simulation is repeated separately with the particles released at the entrance of each stage. In these calculations, particle diameters are specified to match values typically observed in pharmaceutical aerosols (0.5–10 μm). Particle diameters are determined by specifying the proper value of St in Eq. (6).

Fig. 4 shows results from these simulations for each of the six stages considered here. The trapping curves predicted by the simulations are qualitatively identical to the typical S-shaped curves reported in many previous experimental studies. The 50% cut-off diameter (the particle diameter at which 50% of the particles are collected on the plate) predicted by the model is compared with experimental observations in Table 1. Differences

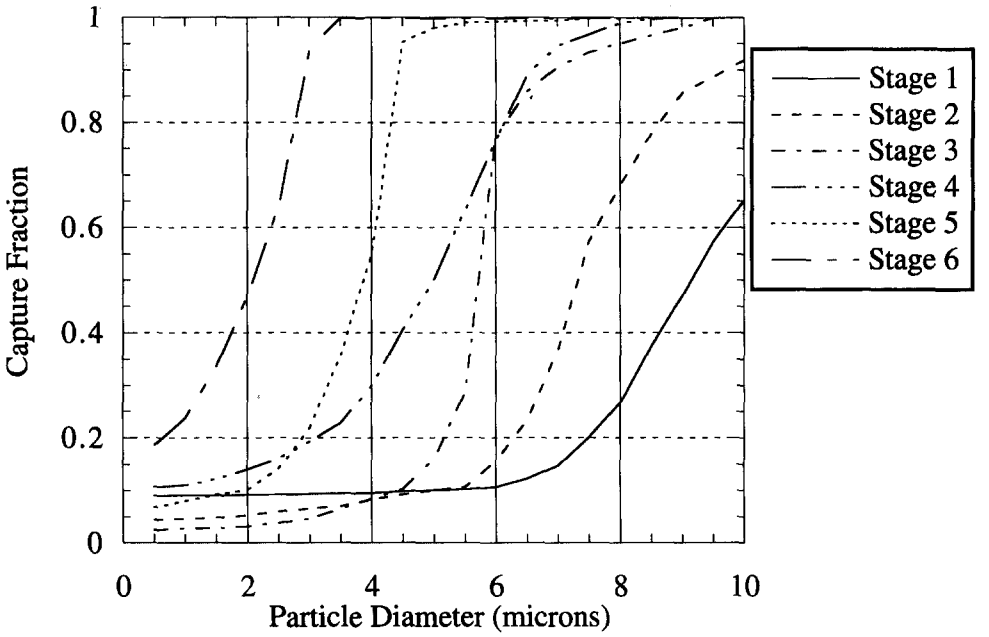

Fig. 4. Trapping efficiency curves for plates 1–6.

between the experimental and computational values are due to round-off errors, truncation in the numerical algorithm, assumptions made in developing the model, differences between the computational and the experimental flow geometries, and 'wall losses'. Considering that 'wall losses' alone can reach 50% of the particles of a given size (Fairchild and Wheat, 1984; Horton et al., 1992), computational results presented in Table 1 should be considered well within experimental error.

Several studies have attempted to model the size distribution of particles that should be trapped in various stages by convoluting trapping efficiency curves corresponding to individual stages. However, a trapping efficiency curve is a measurement obtained under idealized conditions (in particular, under uniform concentration of particles across the jet). As discussed below, the global structure of the flow can introduce non-idealities in particle spatial distribution. Moreover, as shown in Marple's original work (Marple, 1970), the cut-off diameter for a given collection plate depends on where in the cross-section of the entrance the particle is introduced. Unaccounted non-idealities such as 'wall losses' and non-uniformities in the particle concentration can introduce significant errors in the calculated distributions; moreover, such effects can accumulate in the downstream direction due to interaction between events taking place in different stages. To examine such effects, a second set of computations was performed, where 1000 particles of a given size were distributed uniformly across the radius of the first hole and were then followed throughout the device until they reached their final destinations. Results are presented in Fig. 5 for three particle sizes (1 μm, dark gray; 3.16 μm ($10^{1/2}$

Table 1
Comparison of computational and experimental cut-off diameters

Stage	Experimental cutoff diameter (μm)	Computational cutoff diameter (μm)
1	9.2	8.8
2	6.5	7.2
3	4.6	5.8
4	3.2	4.5
5	2.3	3.5
6	1.3	1.8

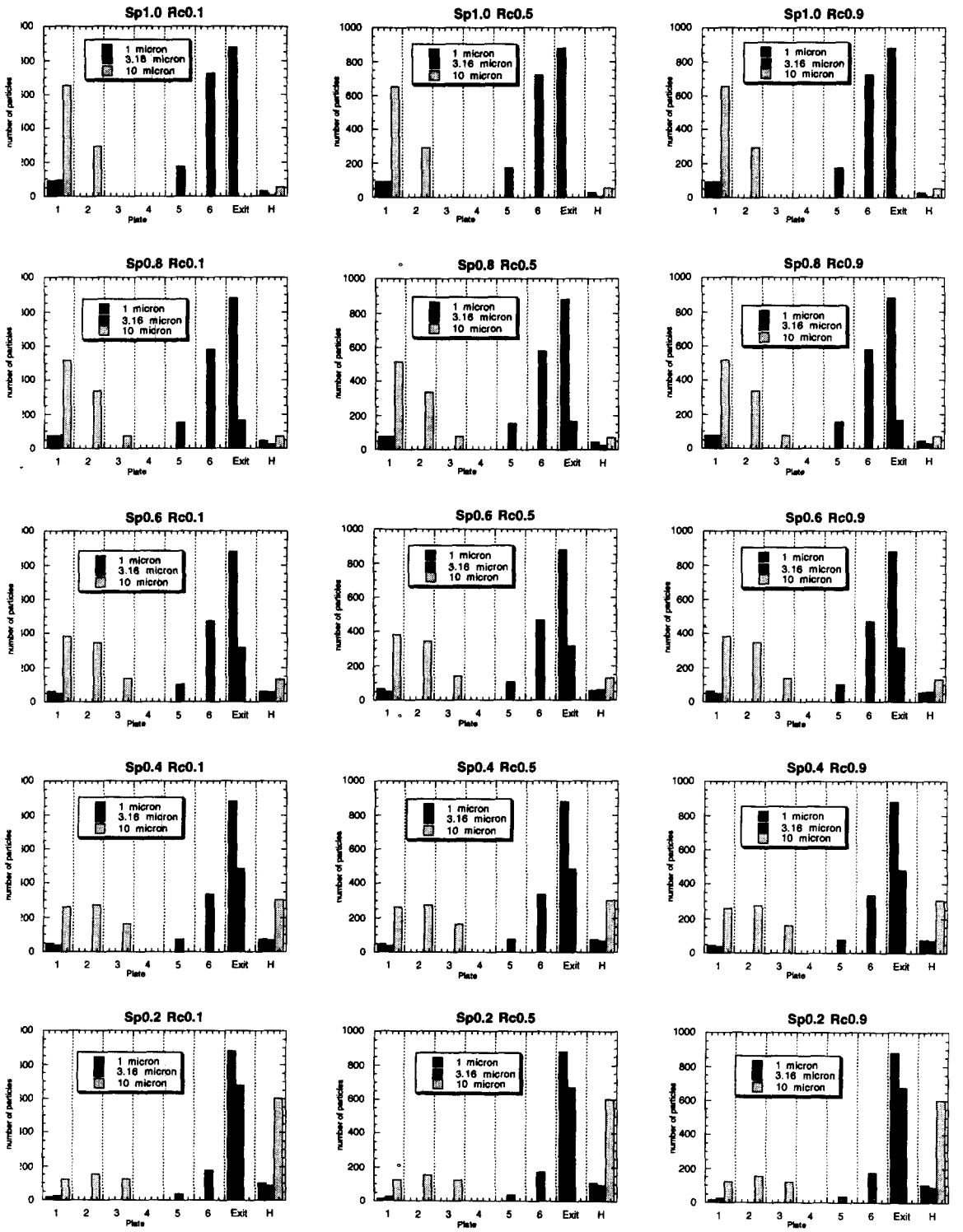

Fig. 5. Histograms indicating the number of particles that are collected in plates 1–6 (bars marked 1–6), particles that leave the impactor (bars marked exit) and particles that are held by the flow (bars marked H). Results are shown for particle diameters equal to 1 μm, 3.14 μm and 10 μm; sticking probabilities equal to 1.0, 0.8, 0.6, 0.4 and 0.2 (from top to bottom); and restitution coefficients equal to 0.9, 0.5 and 0.1 (from left to right).

μm), medium gray; and 10 μm, light gray; i.e. the darker the color, the smaller the particle). The figure shows 15 histograms corresponding to five values of sticking probability (from top to bottom, rows correspond to $p_S = 1.0$, 0.8, 0.6, 0.4, 0.2) and three values of restitution coefficient (from left to right, columns correspond to $R =$ 0.9, 0.5, 0.1). Each histogram shows particles trapped in collection plates 1–6, particles that leave the impactor (bars marked 'exit'), and particles that neither stick to any surfaces nor leave the impactor, but that are held by the flow (bars marked 'H'). All cases correspond to a real time of 1.5 min, which is similar to the manufacturer's recommended assay time.

Fig. 5 shows that (contrary to our early expectations) deposition patterns of particles of all three sizes are largely independent of the value of R. In all cases, the number of particles that reach a given collection plate shows very small variations (less than 1%) for different values of R. Moreover, the effect of R is entirely negligible for high values of p_S. This behavior is reasonable; since the particles considered here are very small (smaller than 10 μm), inertia plays only a minimum role on their motion. After an ineffective collision with a collection plate, particles very quickly adopt the velocity of the surrounding fluid. Hence, the fractional momentum that they retain after the collision is quickly 'forgotten' and plays a negligible role on the subsequent motion of the particles.

Let us now discuss the behavior of 1-μm particles. For $p_S = 1.0$, displayed in the top row in Fig. 5, only the first stage is effective in trapping approximately 9% of such particles. A few particles (less than 1%) are trapped in stage 2. A significant number (88%) of 1-μm particles leave the impactor. The remaining 2–3% of the particles are neither trapped by collection plates, nor do they deposit on other impactor surfaces. They become permanently held in recirculation regions of the flow. This unexpected effect was confirmed by running the simulation for a long time (corresponding to several minutes of real flow) until it reached a 'steady state' in which no more particles deposited on any surface. At this point, the simulation was stopped, and the positions of the particles were plotted. All the 'missing' 1-μm particles were found in stage 1, held in the large recirculation region bounded by the streamline that begins at point C and ends at point D (Fig. 3(c)). Particles that undergo ineffective collisions, and also particles that do not collide at all, are carried out by the flow, and some of them cross the boundary of the recirculation region due to a combination of inertia and gravity. These particles find themselves trapped in stable recirculating orbits and are unable to leave the segregated region. This trapping effect is not unique to 1-μm particles; rather, it affects particles of all sizes, and will be discussed in more detail in the next section, in which deposition patterns are computed for aerosols with continuous particle size distributions.

The sticking probability has a moderate effect on the behavior of 1-μm particles. As p_S decreases, the number of particles collected in stage 1 decreases gradually; for $p_S = 0.2$ (bottom row), only 2% of the particles are captured. Concurrently, the number of particles held in the flow (marked H in Fig. 5) increases, and for $p_S = 0.2$, 10% are held in the recirculating region in stage 1. The number of 1-μm particles that leave the impactor remains unchanged and equal to 88%, suggesting that these particles never collide with any impactor surfaces (and hence, their behavior is unaffected by the value of p_S).

Next, we discuss the behavior of particles with intermediate size equal to 3.16 μm ($10^{1/2}$ μm). The deposition pattern of these particles depends very strongly on p_S. For $p_S = 1.0$ (top row), 10% of these particles deposits in stage 1, 18% are collected in stage 5, 78% are collected in stage 6 and 1% of the particles are permanently held by the flow in stages 1, 5 and 6. No particles are collected in stages 2, 3, or 4, and no particles leave the impactor. However, this behavior changes dramatically as the value of p_S is decreased. For $p_S = 0.2$ (bottom row): only 2% of particles are collected in stage 1; 4% are collected in stage 5; and 18% are collected in stage 6; 8% of these particles are now held in stages 1, 5 and 6; and 68% of them leave the impactor.

Finally, we discuss the behavior of large particles with size equal to 10 μm. These particles behave very differently from the other two cases

discussed above. As expected, they are collected predominantly in the first few stages. For $p_S = 1.0$ (top row), 65% of these particles are collected by stage 1, 30% are collected by stage 2, and the remainder 5% become permanently held in the large recirculation flow regions in stages 1 and 3. The deposition profile is quite steep for high values of p_S (for $p_S \geq 0.6$, the profile of 10-μm particles has a maximum at the first plate) but it becomes increasingly flatter as p_S decreases. For $p_S = 0.2$ (bottom row), only 12% of the particles are collected in stage 1, 16% are collected in stage 2, and 12% are collected in stage 3; the remaining 60% are held in recirculating regions in stages 1 and 3. None of the 10-μm particles leave the impactor for any of the values of p_S examined here.

6. Effects of the particle size distribution

Since only three discrete sizes (1 μm, 3.16 μm and 10 μm) were considered in Section 5, it is possible that many other behaviors were missed by the simulations discussed above. Intermediate particle sizes must be considered in order to determine the range of particle sizes collected in each plate. In this section, we discuss results from simulations considering 50 000 particles with a continuous distribution of sizes so that particles with all diameters in the range 1–10 μm are assigned the same probability. Such simulations are resource-intensive, requiring 50–100 h of CPU time in a SUN SPARC 20-612 workstation, and therefore only three values of p_S (1.0, 0.5 and 0.2) are considered. Since the results discussed so far indicate that R has a negligible effect on the behavior of particles of all sizes, only one value of R ($R = 0.5$) is considered in the remainder of this paper.

Results from a simulation corresponding to $p_S = 1.0$ are shown in Fig. 6(a). The figure shows the normalized particle size distribution (PSD) of particles collected in each plate (Fig. 6(a), left), the spatial locations of particles held in the flow (Fig. 6(a), center), and the PSD of particles held by recirculating regions of the flow (Fig. 6(a), right). PSDs are calculated by dividing the range of particle diameters into 100 'bins' of equal width and then counting the number of particles in each bin. All PSDs are normalized to have the same area under them, facilitating visualization of results in stages with only a few particles. Once again, the PSD of particles collected by the plates strongly resemble those reported in previous experimental studies that focused on a similar impactor (Fairchild and Wheat, 1984; Horton et al., 1992). As expected, the PSD of particles collected in plate 1 (Fig. 6(a), top left) is qualitatively identical to the corresponding trapping curve for plate 1 (Fig. 4). Particles of all sizes are trapped in this stage, but the PSD is dominated by particles with diameters ≥ 8 μm. However, PSDs for plates 2–6 do not resemble the S-curves because large particles are trapped by earlier stages; therefore, PSDs for plates 2–6 all display a maximum. Particles of diameters ≥ 5.8 μm are collected in plate 2, which has a relatively broad PSD with a maximum at 7.5 μm. PSDs for plates 3–6 are narrow, indicating that these plates collect only particles within a narrow range of diameters. The modes of these PSDs are close to the thresholds computed in Table 1. Some particles with diameters ≤ 2.5 μm escape the impactor. However, a significant number of particles are held in recirculating regions of the flow in stages 1 and 3 (Fig. 6(a), center). Particles of all sizes are held in stage 1 (Fig. 6(a), top right). As the air jet is deflected by plate 1, particles that miss the plate gain momentum in the radial direction. Inertia carries many of these particles deep into the large recirculating vortex described in Fig. 3(c). Some particles become trapped within the vortex and are unable to leave. The PSD of the particles held in the recirculating region in stage 1 has a mode of approximately 7.6 μm (Fig. 6(a), top right) and overlaps closely with the PSD of particles collected in plate 2. Particles held in stage 3 have a narrow PSD with a mode of approximately 5 μm. Unless this trapping effect is either avoided (by appropriate flow design) or discounted (by careful calibration), it would introduce an error in the overall PSD determined by the impactor.

Results corresponding to $p_S = 0.5$ are shown in Fig. 6(b). Once again, the PSD of particles collected in plate 1 (Fig. 6(b), top left) resembles the

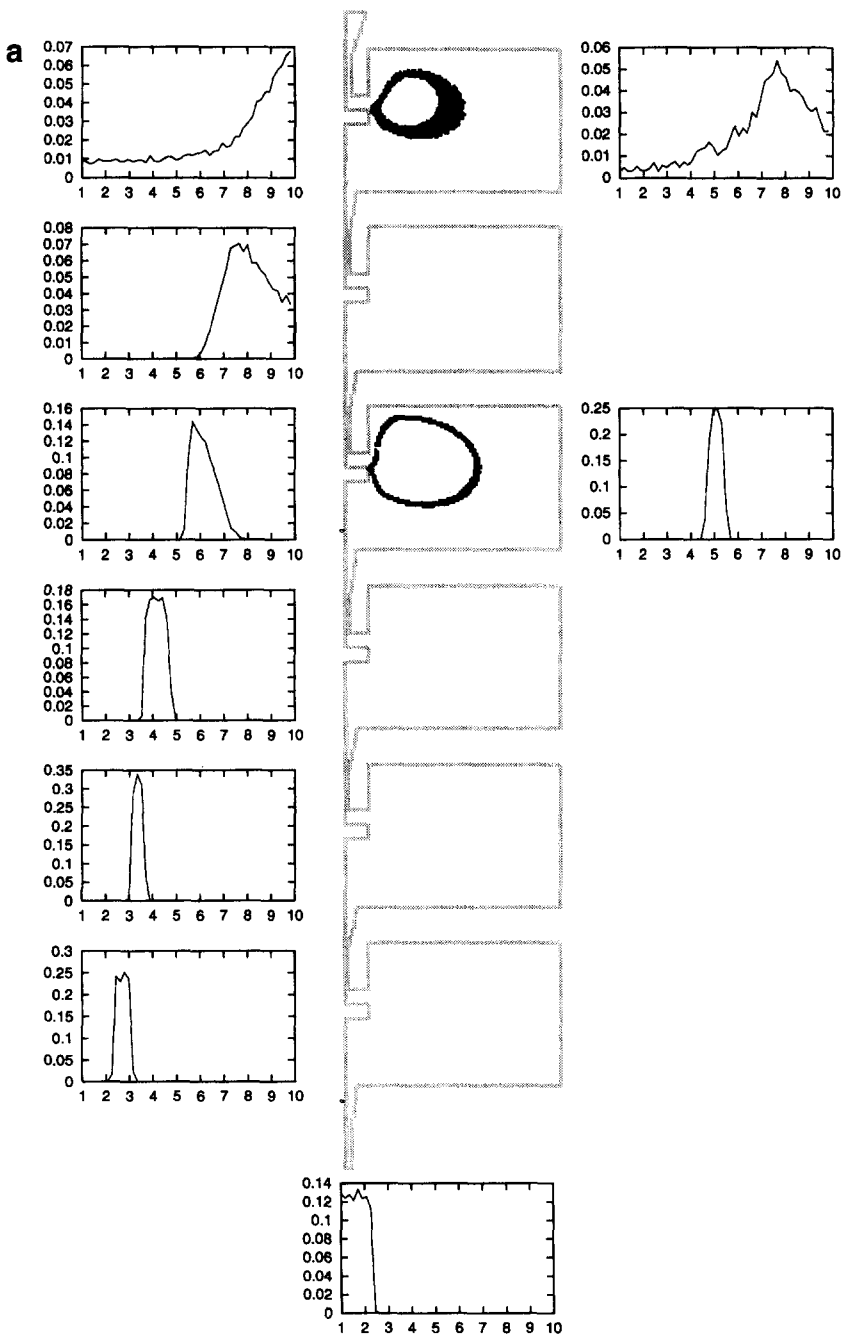

Fig. 6. Results of a simulation considering 50 000 particles with a uniform distribution of sizes. The figure shows the PSD of particles collected in each plate (left), the spatial location of particles held by the flow (center), and the PSD of particles held in each stage (right). (a) $p_S = 1.0$, (b) $p_S = 0.5$, (c) $p_S = 0.2$.

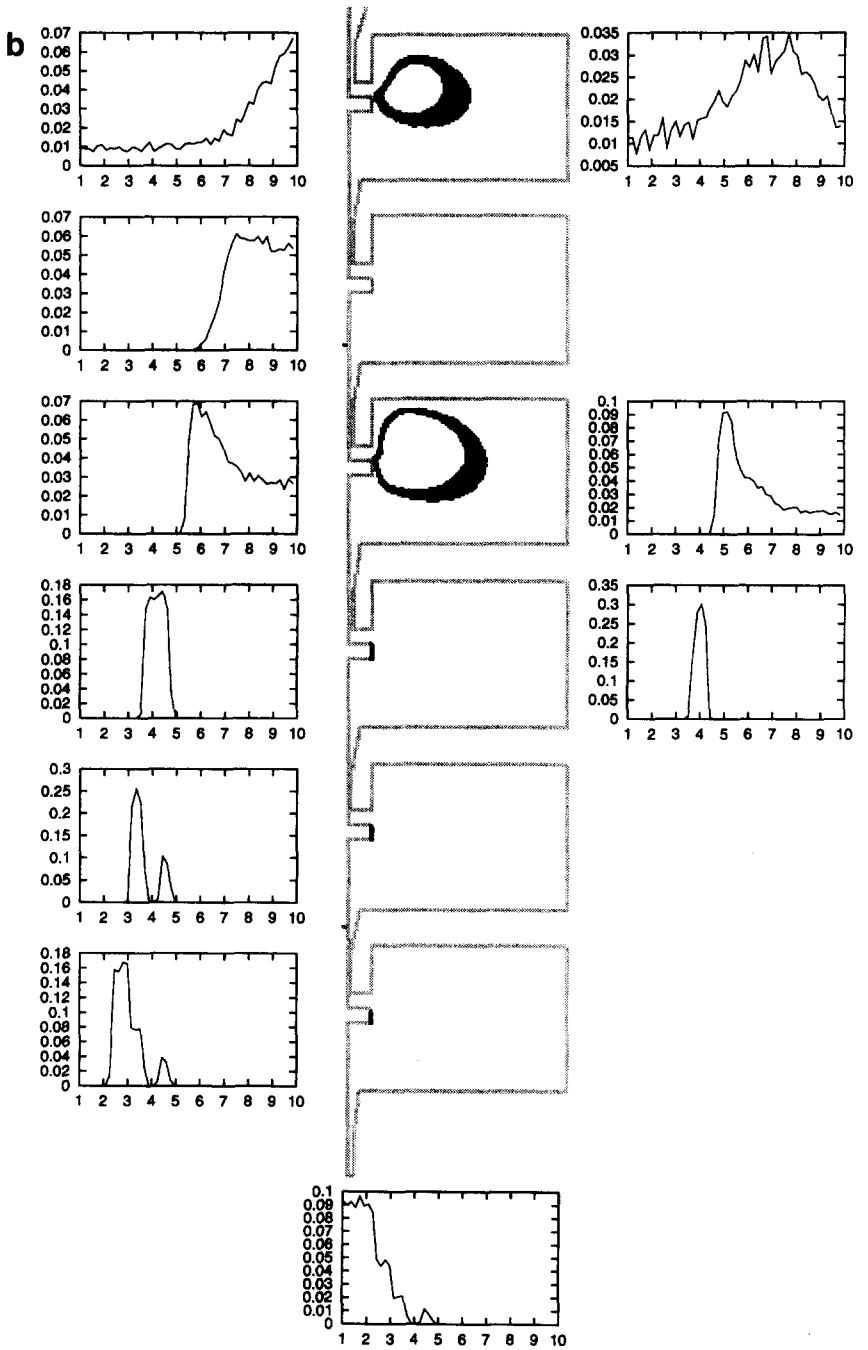

Fig. 6(b).

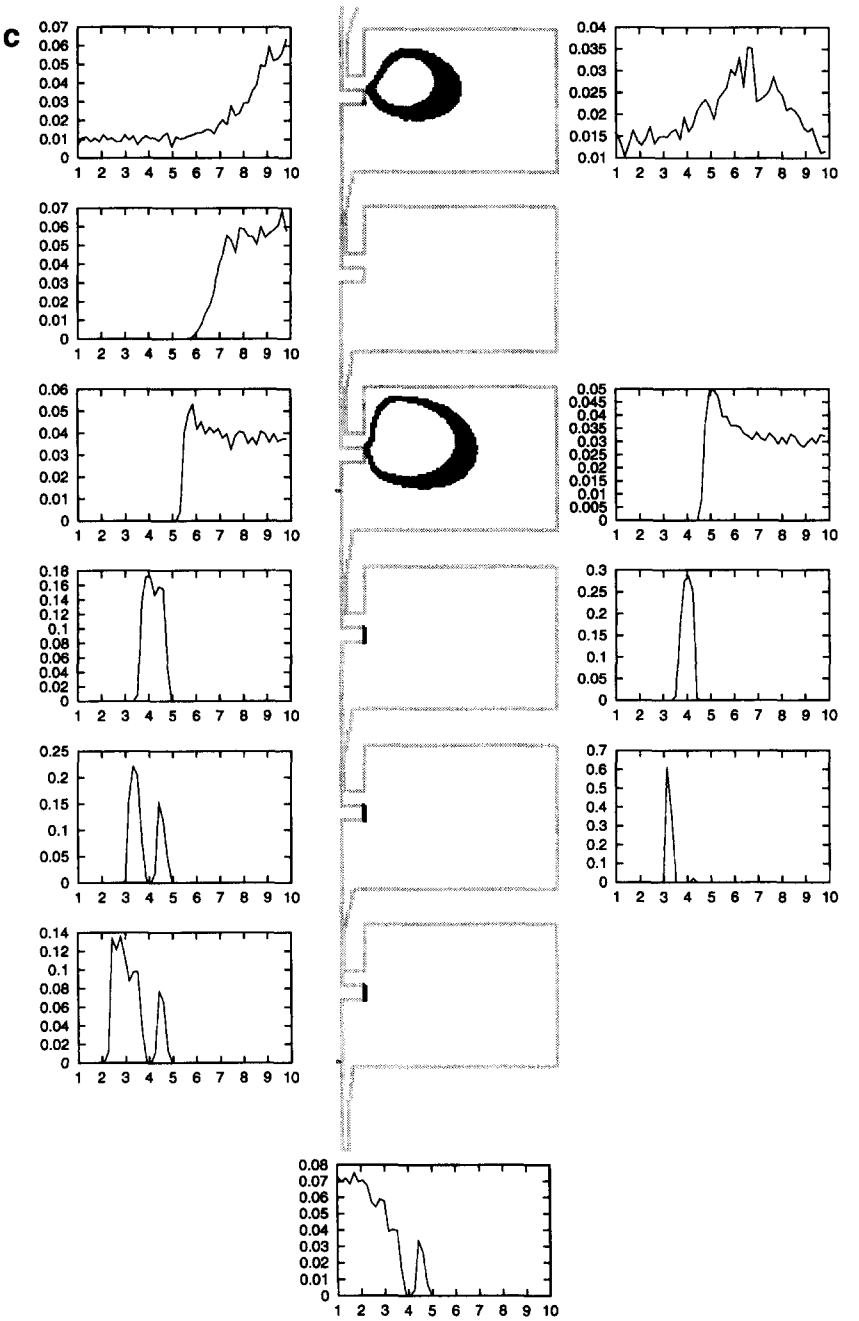

Fig. 6(c).

corresponding trapping efficiency curve (Fig. 4(a)). However, since the plate is only half as effective as it was in Fig. 6(a), many large particles that would have been collected in this plate now proceed further into the impactor, and the PSDs for plates 2 and 3 now display many large particles. The PSD for plate 4 is identical to the one observed for $p_S = 1.0$, but since the plate is only half as efficient as before, many particles that would have been collected by this plate now also proceed further downstream. Such particles appear as a secondary peak of approximately 4.5 μm in the PSDs for plates 5 and 6 and also in the PSD of particles that leave the impactor. Similarly, particles with diameters of approximately 3.5 μm that would have been collected in plate 5 now appear in the PSD for plate 6 and in the PSD of particles that leave the impactor.

As p_S is reduced, the number of particles held in the flow increases considerably. Once again, particles are held in recirculating flow regions in stages 1 and 3. While the PSD of particles held in stage 1 is similar to the PSD obtained in the previous case, the PSD of particles held in stage 3 shows a significant number of large particles. In fact, this recirculating region acts as a virtual impactor (Hounam and Sherwood, 1965; Conner, 1966; Marple and Chien, 1980) for particles with diameters ≥ 5 μm, since no such particles get past this stage. A consequence of this efficient trap is that, as mentioned above, the PSD of particles collected in plate 4 is identical to the one observed in Fig. 6(a) for $p_S = 1.0$. Particles are also held in stagnant regions of the flow in stages 4, 5 and 6 (Fig. 6(b), center). These stagnant regions are located at the side of the collection plate and are caused by a balance of the forces imposed on particles by the flow (which in such locations is vertical and in the upward direction) and by gravity (which is also vertical but in the downward direction). For some specific particle sizes these forces are evenly matched; such particles are held in the stagnant regions and are unable to leave. The PSD of particles held in the stagnant region in stage 4, displayed in Fig. 6(b) (lower right), is narrow and has a mode of approximately 4 μm. The number of particles held in stagnant regions in stages 5 and 6 was small and insufficient to compute meaningful PSDs.

All these trends are further confirmed in Fig. 6(c), which shows results corresponding to $p_S = 0.2$. Once again, the PSD for plate 1 remains unchanged, but as the number of large particles collected by plate 1 decreases, the maximum in the PSD for plate

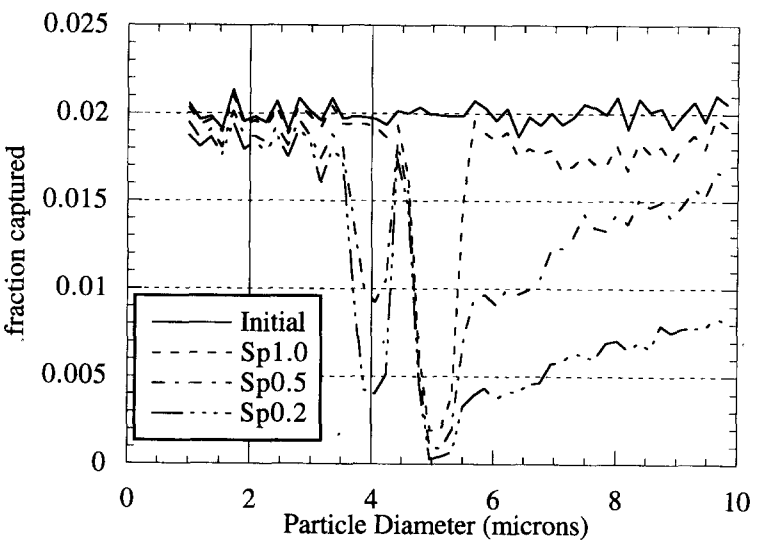

Fig. 7. Comparison of the PSD entering the device with the cumulative PSDs of particles either collected in plates 1–6 or leaving the impactor.

2 shifts to larger diameters ($\approx 9.6\ \mu$m). The PSD for plate 3 is now very broad and flat and displays many particles that have escaped plates 1 and 2. The effects of large particles moving further downstream are also evident in the PSDs for plates 4–6. The PSD of particles that leave the impactor (center, bottom) now shows a significant number of particles in the 4–5 μm range. As before, particles are trapped in recirculating flow regions in stages 1 and 3, but the number of such particles is now considerably larger. The recirculating region in stage 3 remains a perfect trap for particles with diameters of $\geq 5\ \mu$m. As before, particles with diameters of approximately 4 μm are trapped in a stagnant region in stage 4, and particles with diameters of approximately 3.2 μm are trapped in a stagnant region in stage 5. PSDs for such particles are displayed in Fig. 6(c).

Since all of the PSDs in Fig. 6 are normalized, the figure does not provide a clear indication of the relative prevalence of particles held in recirculating and stagnant regions of the flow. This issue is addressed in Fig. 7, which compares the PSD of all particles entering the impactor (given by a solid horizontal line) with the 'overall' PSD of particles either collected in stages 1–6 or leaving the impactor. Such overall PSD is an approximation of the PSD that would be measured by the device considered in our simulations. The difference between the overall PSD and the true PSD is the error caused by particles held up by the flow. For $p_S = 1.0$, a relatively small error occurs for particles of all sizes, except for particles with diameters of approximately 5 μm. All such particles are held in stage 3, which results in a large error. When $p_S = 0.5$, errors increase substantially for all particles with diameters $\geq 5\ \mu$m, which are held up in recirculating regions in stages 1 and 3, and for particles with diameters of approximately 4 μm, which are held in a stagnant region in stage 4. All of these errors are even larger for $p_S = 0.2$, because a significant number of particles of all sizes are held by the flow. This trapping effect provides an alternative explanation for the 'wall losses' reported in previous studies (Fairchild and Wheat, 1984; Horton et al., 1992); once the flow is interrupted, particles held in recirculation regions would fall onto walls, where they would be reported as 'wall losses'. In the impactor considered in these simulations, this effect is highly dependent on particle diameter and would be significant for particles with diameters $> 3\ \mu$m.

7. Conclusions

Numerical techniques have been used in this paper to obtain a detailed description of the motion and deposition of particles in a cascade impactor. The geometry of the case study considered here is a six-stage impactor similar to the first six stages of the PC-2 impactor manufactured by California Instruments. The numerical model was validated by computing trapping efficiency curves that closely resemble those reported in previous literature. Subsequently, the model was used to consider the effects of impactor geometry, sticking probability, restitution coefficient and particle size on the fate of particles as they move through the impactor. The restitution coefficient was found to have a negligible effect. Simulations correctly predicted that for high sticking probability, the impactor behaves as an effective classification device; particles within narrow ranges are collected by each plate. For low sticking probabilities, the ranges of particles collected in each plate become considerably broader.

It was also shown that the global flow in the impactor can play a significant and previously unexplored role. Particles can become held in recirculating and stagnant regions of the flow; the number of such particles can be large for low sticking probabilities. Since such particles would not be considered in the analysis of results produced by the device, this trapping phenomenon would introduce errors in the experimentally determined particle size distribution. Likely, such errors account for many of the 'wall losses' reported in previous literature. This effect, which is caused entirely by the structure of the flow inside the impactor chambers, could be easily remedied by introducing minor alterations to the design of impactor chambers.

Several issues that remain unresolved deserve to be mentioned here. The trapping effect discussed here needs to be verified by flow visualization experiments conducted under carefully controlled conditions. The model could be expanded to include Brownian motion of the particles, sticking probabilities that depend on particle size and/or particle

momentum, and three-dimensional time-dependent flow fluctuations ensuing from hydrodynamic instability. It would also be interesting to consider other flow rates and to compare numerical results for impactors of different geometries. These and other issues will be addressed in future publications.

References

Bird, R.B., Stewart, W.E. and Lightfoot, E.N., *Transport Phenomena*, Wiley, New York, 1960, Ch. 3.

Conner, W.D., *J. Air Pollut. Control Assoc.*, 16 (1966) 35.

Dahneke, B., *Aerosol Sci. Technol.*, 23 (1995) 25.

Druzhinin, O.A., Ostrovsky, L.A. and Stepanyants, Y.A., *Chaos*, 3 (1993) 359.

Dunn, P.F., Brach, R.M. and Caylor, M.J., *Aerosol Sci. Technol.*, 23 (1995) 80.

Dupont, V., Pourkashanian, M., Williams, A. and Woolley, R., *Fuel*, 72 (1993) 497.

Fairchild, C.I. and Wheat, L.D., *Am. Ind. Hyg. Assoc. J.*, 45 (1984) 205.

Fults, C., Cyr, T.D. and Hickey, A.J., *J. Pharmacol.*, 43 (1991) 726.

Goto, Y., Abe, T. and Fujiwara, K., *Diesel Engine Research*, Part 2, Society of Automotive Engineers, Warrendale, PA, 1987.

Hecht, L. and Cibulsky, M., *Print. Circuit Fabrication*, 15 (1992) 34.

Her, J.Y. and Kim, S.S., *Aerosol Sci. Technol.*, 14 (1991) 157.

Hering, S.V., *Aerosol Sci. Technol.*, 7 (1987) 257.

Hinds, W.C., Liu, W.C. and Froines, J.R., *Am. Ind. Hyg. Assoc. J.*, 46 (1985) 517.

Holzner, P.M. and Muller, B.W., *Int. J. Pharm.*, 116 (1995) 11.

Horton, K.D., Ball, M.H.E. and Mitchell, J.P., *J. Aerosol Sci.*, 23 (1992) 505.

Hounam, R.F. and Sherwood, R.J., *Am. Ind. Hyg. Assoc. J.*, 26 (1965) 122.

John, W., *Aerosol Sci. Technol.*, 23 (1995) 2.

Jurcik Jr., B.J., Brock, J.R. and Trachtenberg, I., *J. Aerosol Sci.*, 20 (1989) 701.

Liu, M. and Peskin, R.L., *ASME* 166 (1993) 95.

Luczynska, C.M., Li, Y., Chapman, M.D. and Platts-Mills, T.A.E., *Am. Rev. Respir. Dis.*, 141 (1990) 361.

Marple, V.A., Thesis, University of Minnesota, USA, 1970.

Marple, V.A. and Chien, C.M., *Environ. Sci. Technol.*, 14 (1980) 976.

Marple, V.A. and Liu, B.Y.H., *J. Colloid Interface Sci.*, 53 (1974) 31.

Marple, V.A., Rubow, K.L. and Behm, S.M., *Aerosol Sci. Technol.*, 14 (1991) 434.

Maxey, M.R. and Riley, J.J., *Phys. Fluids*, 26 (1983) 883.

May, K.R., *J. Sci. Instrum.*, 22 (1945) 187.

Natusch, D.F.S. and Wallace, J.R., *Atmos. Environ.*, 10 (1976) 315.

Ondov, J.M., Ragaini, R.C. and Biermann, A.H., *Atmos. Environ.*, 12 (1975) 1175.

Rader, D.J. and Marple, V.A., *Aerosol Sci. Technol.*, 4 (1985) 141.

Sazhin, S., Leys, C., Toebaert, T. and Sazhina, E., *J. Phys. D: Appl. Phys.*, 26 (1993) 1872.

Sommerer J.C. and Ott, E., *Science*, 259 (1993) 335.

Stoer, J. and Bulirsch, R., *Introduction to Numerical Analysis*, Springer-Verlag, New York, 1980.

Tio, K.-K., Linan, A., Lasheras, J.C. and Ganan-Calvo, A.M., *J. Fluid Mech.*, 254 (1993) 671.

Tsai, C.-J. and Cheng, J.-H. *Aerosol Sci. Technol.*, 23 (1995) 96.

Vaughan, N.P., *J. Aerosol Sci.*, 20 (1989) 67.

Wang, L.P., Maxey, M.R., Burton, T.D. and Stock, D.E., *Phys. Fluids A*, 4 (1992) 1789.

Xu, M., Willeke, K., Biswas, P. and Pratsinis, S., *Aerosol Sci. Technol.*, 18 (1993) 143.

Yang, D.Y., Ou, J.J., Heist, R.H., Chen, S.H., Dukat, A.J. and Eberle, A.C., *Ind. Eng. Chem. Res.*, 32 (1993) 1727.

Yu, L., Ott, E. and Chen, Q., *Physica D*, 53 (1991) 102.